Article:

Magnus, C., Cooper, D., Jantzen, C. et al. (3 more authors) (2021) Synthesis and high temperature corrosion behaviour of nearly monolithic Ti3AlC2 MAX phase in molten chloride salt. Corrosion Science, 182. 109193. ISSN 0010-938X

https://doi.org/10.1016/j.corsci.2020.109193

Synthesis and High Temperature Corrosion Behaviour of Nearly Monolithic Ti_3AlC_2 MAX Phase in Molten Chloride Salt

Carl Magnus[a,*], Daniel Cooper[a,b], Craig Jantzen[c], Hugues Lambert[d], Tim Abram[c], Mark Rainforth[a]

[a]*The Henry Royce Institute and Department of Engineering Materials, The University of Sheffield, Sir Robert Hadfield Building, Sheffield, S1 3JD, UK*

[b]*Seaborg Technologies, Titangade 11, 2200, Copenhagen, Denmark*

[c]*Department of Mechanical, Aerospace and Civil Engineering, University of Manchester, UK*

[d]*Department of Chemical Engineering and Analytical Science, University of Manchester UK*

Abstract

Nearly monolithic MAX phase containing 95 wt.% Ti_3AlC_2 and 5 wt.% TiC_x was synthesized by spark plasma sintering under vacuum sintering conditions. Corrosion behaviour of Ti_3AlC_2 was investigated in molten LiCl–KCl salt at 600 °C under a dry Ar atmosphere. Evolution of microstructure and surface chemistry of the exposed sample was characterized by scanning electron microscopy (SEM), X-ray diffraction (XRD) and glancing angle X-ray diffraction (GAXRD). Results showed that Al dissolution led to delamination of the layered structure which favoured the ingress of chlorine and its subsequent intercalation into the Al–site plane to form a $Ti_3C_2Cl_2$ exfoliation layer. De-twinning of the Ti_3C_2 layers possibly due to Cl^- anions substitution by O results in non-stoichiometric $TiC_{0.67}$ formation.

Keywords: MAX Phase; Spark Plasma Sintering; Molten Salt Reactor; De-intercalation; De-twinning; Exfoliation

1. Introduction

Molten salt reactors (MSRs) are nuclear reactors characterized by the use of a fluid fuel in the form of a molten chloride or fluoride salt as coolant rather than the solid fuel employed in most reactors. MSRs are currently gaining wide interest because of a number of key benefits, including but not limited to [1, 2]: (1) atmospheric pressure operation, (2) high degree of passive safety, (3) high thermal efficiency linked to high volumetric heat capacity and thermal conductivity of the molten salts, (4) high solubility of most fission products in molten salts, and (5) lower spent fuel per unit energy. However, the molten salts utilized are quite corrosive to structural alloys being considered for molten salt reactors. As a result, the corrosion resistance of structural alloys employed in MSRs plays an important role in their fruition [3, 4]. The protective oxide scale that is heavily relied upon for corrosion protection in high temperature environments is essentially unstable in molten fluoride and/or chloride salts [5]. This is because alloying elements in most MSR structural alloys (particularly chromium added for oxidation protection) are susceptible to dissolution in the molten salts and as such may lead to thinning of the structural component [3]. Evaluation tests of prospective structural materials in fluoride salt systems indicate that nickel-based alloys are the best of the commercially available alloys. This is because nickel itself is very stable in molten chlorides and fluorides because of the low Gibbs free energy of formation of the nickel chloride and fluoride species [4]. However, the presence of an appreciable amount of Cr such as in Inconel alloys renders the alloy susceptible to attack by the circulating molten salts at the MSR temperature via the selective removal of Cr [6]; however, some Cr is necessary to maintain oxidation resistance on the outer face of the materials [6]. On the other hand, substituting Cr with Mo such as in Hastelloy B presents excellent corrosion resistance in molten halide salts even at temperatures in excess of 871°C. However, the drawbacks with Hastelloy B are its susceptibility to grain boundary embrittlement by fission products [3, 7], its poor oxidation resistance, and poor fabricability. Hastelloy-N, which was specifically developed for molten fluoride salts during the Molten Salt Reactor Experiment (MSRE) program has shown good compatibility with molten fluoride salt and acceptable oxidation resistance in air [8, 9]. However, investigators have reported that Hastelloy-N, a low Cr-content alloy with Mo, is susceptible to intergranular corrosion via the continuous depletion of Cr and Mo – with the depth and extent of corrosion increasing with temperature [3, 7, 10].

As there are at least two families of salt employed in MSRs, a single alloy is not likely to meet all requirements and material challenges (irradiation effects, corrosion, and elevated temperature strength) for potential designs [11]. These have led to active consideration of new structural materials such as MAX phases for use in various reactor components and designs. An additional benefit of MAX phases is their low neutron absorption (depending on MAX phase elemental composition, but particularly for $Ti_{n+1}(Al/Si)C_n$ MAX phase system as well as Zr and Nb-based MAX phases) [12-14].

MAX phases are a family of layered hexagonal nano-laminated (adopt the $P6_3/mmc$ symmetry) with two formula units per unit cell and are governed by the general formula $M_{n+1}AX_n$, where M is an early transition metal, A is an A-group element, X is carbon and/or nitrogen and $n = 1$, 2, 3 or higher [15]. They combine simultaneously properties of both ceramics (that is, oxidation resistance, high temperature strength, wear resistance and high elastic modulus) and metals (such as, good electrical and thermal conductivity, machinability, low hardness, thermal shock resistance and damage tolerance) making them highly attractive as potential structural materials in various applications [12, 16-18]. Previous studies have shown that some MAX phases are suitable for nuclear applications [13, 14, 19, 20], as they can withstand extreme temperatures, elevated irradiation dose whilst maintaining crystallinity, and resistance to chemical attacks from corrosive coolants [21].

Titanium aluminium carbide (Ti_3AlC_2) is a member of the series $Ti_{n+1}AlC_n$ (n = 2) – and represents one of the most studied members of the MAX phases. The Ti_3AlC_2 crystal structure is composed of individual Ti_3C_2 layers separated by Al atoms. The chemical bonding in Ti_3AlC_2 is anisotropic and metallic-covalent-ionic in nature, with the metallic and covalent contribution reported to be dominant [22]. The unusual bonding and anisotropic structural characteristics are responsible for the unique metalloceramic properties reported in MAX phase material [23]. It has excellent oxidation resistance which stems from the formation of dual-layered dense and adherent passivating films consisting of an inner continuous layer of alpha-Al_2O_3 and an out layer TiO_2 (rutile) [24-26]. Ti_3AlC_2 shows good irradiation resistance by undergoing irradiation hardening via the evolution of irradiation defects acting as obstacles to dislocation glide [14]. It has been reported that Ti_3AlC_2 exhibits excellent corrosion resistance to alkali solution at room and elevated temperature [26, 27]. Corrosion behaviour of Ti_3AlC_2 in 3.5 % NaCl solution at room temperature was studied by Zhu et al. It was shown that the lamellar microstructure of Ti_3AlC_2 provided a diffusion path for the outward diffusion of Al – this deteriorated the passivating efficiency making it susceptible to inward-diffusing corrosive species [28]. Another study on the suitability of MAX phases in in-core nuclear plant applications and neutron transmutation behaviour showed that, Ti_3AlC_2 is damage tolerant in terms of creep and thermal/mechanical fatigue – whilst maintaining a high degree of compatibility with molten lead and sodium coolants [12].

Whilst the literature on the corrosion behaviour of MAX phases in chloride and/or fluoride salt at elevated temperature is sparse, some studies have been reported. Ling et al.[29] investigated the corrosion of Ti_3AlC_2 and Ti_3SiC_2 in molten LiF-NaF-KF salt. The results from their work revealed undesirable selective removal of the A-element leaving behind cubic formation of TiC_x. Albeit both MAX phases reported to be susceptible to corrosion via the loss of the A–element; the entire loss of the intercalated Al within the Ti_3C_2 layers was reported for Ti_3AlC_2. In another study, Naguib et al. [30] reported the topotactic transformation of Ti_2AlC by de-twinning into Ti-C-O-F following the outward diffusion of Al when heated in molten fluoride in air.

The scope of this work was to synthesize Ti_3AlC_2 MAX phase via the elemental powder route using spark plasma sintering (SPS) and study the corrosion behaviour in molten chloride salt at elevated temperature [31]. Understanding the passivation and corrosion behaviour in chloride salt at high temperature will help to elucidate the corrosion mechanism and the suitability of MAX phases as a structural material in molten salt reactors (MSR).

2. Materials and methods

2.1. Materials

Polycrystalline bulk Ti_3AlC_2 was synthesized using starting elemental powders of Ti (-100 mesh, 99.7 % purity, Aldrich), Al (-200 mesh, 99 % purity Acros Organics) and graphite powder (general purpose grade, Fischer Chemical) as precursors to produce the target specimen. Titanium and graphite powders were milled in a SPEX 8000M Mixer/Mill for 2 hours and then mixed with 1.0 parts of aluminium. The mixed powder was then poured into a graphite die (20 mm in diameter). The loaded powder was separated from the graphite die by a boron nitride-sprayed 0.2 mm-thick graphite foil. The punches were also BN-sprayed to avoid welding at high temperature. The mould-powder-punch assembly was then covered with graphite felt to prevent heat dissipation. Synthesis was carried out using spark plasma sintering (SPS) in an FCT Systeme HP D 25 furnace unit under vacuum. Synthesis was carried out at 1350 °C with an applied pressure of 50 MPa. The heating rate was maintained at 50 °C/min up to the requisite sintering temperature and held for 15 min before the SPS system was switched off and pressure was released as the sintered compact cools down to room-temperature. Afterwards, the SPSed bulk sample was ground to completely remove the graphite foil adhered to the surface during sintering – and the both sides of the bulk sample were mirror-polished.

2.2. Methods

2.2.1. Phase identification and morphology characterization

The crystalline phases present in the mixed raw powder prior to synthesis and the bulk sample following SPS were analysed by XRD (Panalytical X′Pert^3 diffractometer) with a 0.25° divergence slit and a step size of 0.01° at 2θ. XRD of the air sensitive milled powders was performed under Kapton film. Rietveld refinement was conducted on the XRD pattern collected at $5^\circ \leq 2\theta \leq 120^\circ$ using GSAS and EXPGUI. The density of the polished sintered disc was determined using Archimedes in water and theoretical density obtained using the rule of mixture upon determination of the constituent phases in the bulk sample from the Rietveld refinement data. Microstructural investigation was carried out using scanning electron microscopy (SEM, FEI Inspect F50, The Netherlands) equipped with an X-max 80 mm^2 silicon EDS detector (Oxford Instrument, UK). Glancing angle X-Ray diffraction was performed using a Panalytical X'Pert^3 diffractometer with the glancing angle, ω (in °), varied between 0.5° and 10°.

2.3. Corrosion test

The bulk sample was cut into bars and the cut faces were polished to 3 µm. The samples were exposed in individual alumina crucibles containing 16.1 g of LiCl (Alfa Aesar, > 99 %) and 18.9 g of KCl (Sigma Aldrich, > 99 %), that is, LiCl (59.2 wt.%) and KCl (40.8 wt.%) eutectic salt composition. To maximise the exposed surface area, the bars were suspended by nickel wire from a steel bar. The crucibles were placed in a custom-designed vessel which enabled exposure to be carried out under a dry argon atmosphere (99.998 % Ar passed through an Oxiclear^{TM} oxygen and moisture trap). Further details regarding the custom-designed vessel is reported elsewhere [32]. The furnace temperature was raised to 200 °C at a rate of 5 °C min^{-1} and held for 2 h to dry the salt. The temperature was then raised further to 600 °C and held for 125 h before cooling naturally to room temperature. The salt was removed by dissolution in warm water, following which the samples were washed in distilled water then isopropanol in an ultrasonic bath.

3. Results and discussion

3.1. Phase identification and analysis

Following SPS, the synthesized disc was ground and polished down to 1 µm using diamond paste to ensure the complete removal of the adhered graphite foil layer at the surface. The refined XRD pattern taken from the top surface of the polished and unetched disc is shown in Fig. 1. As shown, the main phase is Ti_3AlC_2 whilst some minor amount of TiC_x coexists as an ancillary phase. The fraction of the phases following quantitative phase analysis by Rietveld refinement were 95 wt.% Ti_3AlC_2 and 5 wt.% TiC_x, respectively.

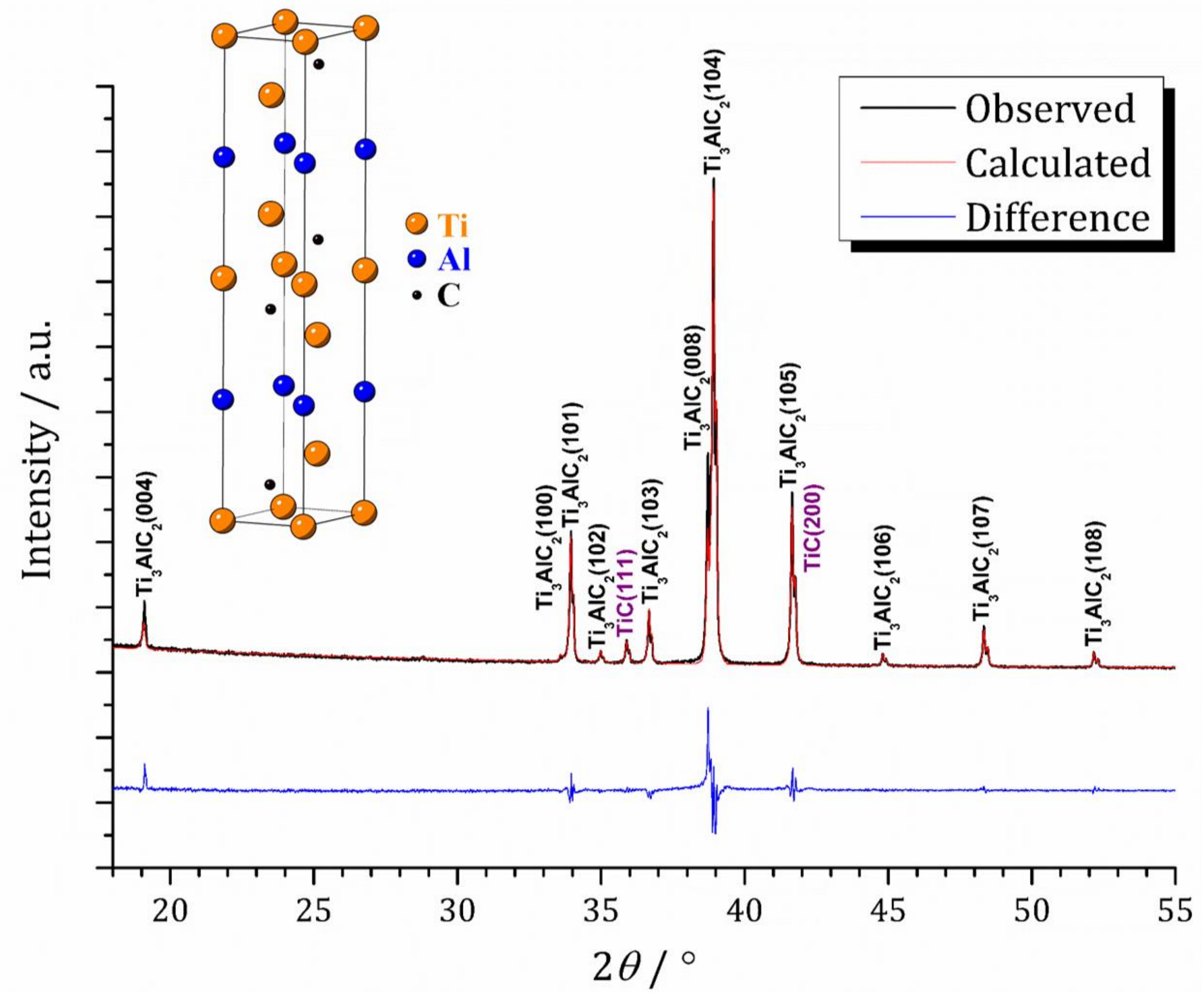

Fig. 1. XRD pattern (black) and the refinement (red) of the SPSed disc. The obtained Rietveld refinement parameters were: $\chi2 = 3.357$; $Rp = 0.082$; and $wRp = 0.109$, respectively. Inset shows the hexagonal crystal structure of Ti_3AlC_2.

The evolution of the ancillary phase TiC_x could be linked to possible de-intercalation of Al following outward diffusion of Al at high temperature and/or the high vacuum employed in SPS drawing out the vapour of Al due to its high vapour pressure. The loss of Al by evaporation will lead to a phase transformation from hexagonal Ti_3AlC_2 ($TiAl_{0.33}C_{0.67}$) to sub-stoichiometric cubic TiC_x according to the chemical reaction [33]:

$$\mathrm{TiAl}_{0.33}\mathrm{C}_{0.67} \rightarrow \mathrm{TiC}_{0.67} + 0.33\mathrm{Al}(\uparrow)$$

An orientation relationship has been reported between TiC and Ti_3AlC_2 as their interface forms a coherent boundary [34]. This implies that an impure Ti_3AlC_2 sample containing TiC_x can initially be prepared, followed by intercalation of Al into the TiC_x inclusions – this will bring about a phase transformation from cubic TiC_x to hexagonal Ti_3AlC_2. This could be a novel route to synthesize a monolithic Ti_3AlC_2 if an optimized sintering parameter and method can be established.

3.2. Microstructural evolution

Fig. 2(a) shows a high-magnification top-surface backscattered scanning electron micrograph revealing the general characteristic microstructures of the polished and unetched bulk sample. According to the elemental EDS analyses obtained from points numbered in the electron micrograph (Fig. 2(b)), the grey phase is the Ti_3AlC_2 with signature plate-like microstructure whilst the bright phase is the TiC_x phase. The TiC_x inclusions appear to cluster and not homogeneously distribute in the Ti_3AlC_2 matrix. The large and elongated grain size of the Ti_3AlC_2 grains seems to play a major role – as Ti_3SiC_2, which often forms a finer grain, has inclusions distributed homogenously within the matrix as observed elsewhere [35, 36].

Some pores (black spots) resulting from grain pull-out due to the metallographic grinding and polishing can be seen on the surface. In general, the sample was fully dense as the measured density was 4.276 ± 0.002 corresponding to an excess of 99 % relative density using the rule of mixture and taking into account the phase fractions. The observed pores due to grain pull-out is not expected to influence the corrosion response and/or the underlying corrosion mechanism.

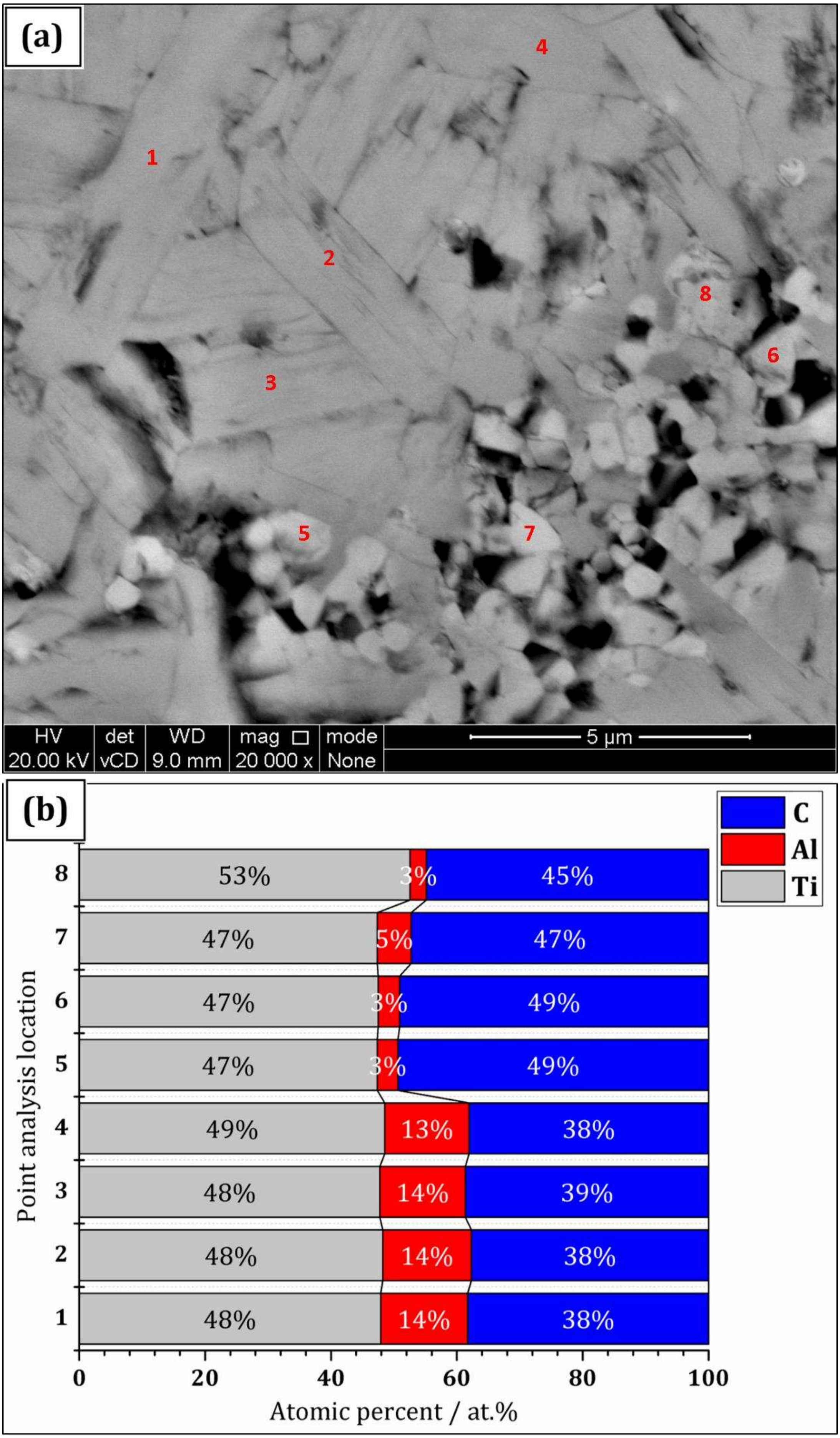
(a)
1
2
3
4
5
6
7
8
HV 20.00 kV
det vCD
WD 9.0 mm
mag ☐ 20 000 x
mode None
5 µm
(b)
C
Al
Ti
8
53%
3%
45%
7
47%
5%
47%
6
47%
3%
49%
5
47%
3%
49%
4
49%
13%
38%
3
48%
14%
39%
2
48%
14%
38%
1
48%
14%
38%
Point analysis location
0
20
40
60
80
100
Atomic percent / at.%

Fig. 2. (a) Backscattered scanning electron micrograph obtained from the top-surface of the polished sample with grey phase corresponding to the Ti_3AlC_2 phase and the bright phase is the TiC_x phase, and (b) semi-quantitative EDS point elemental analyses obtained from the numbered points in the electron micrograph.

3.3. Post corrosion sample status, microstructure and evolution of surface chemistry

At the end of the exposure test the melt was cooled, trapping the sample inside the solidified chloride. The chloride salt was then removed by placing the crucible under running tap water. Sample was not washed in ultrasonic bath because this might remove the corrosion layer; and the priority of this work is to keep the corrosion layer intact so as to determine the corrosion mechanism rather than an accurate corrosion rate. The sample appeared intact as there were no signs of spalling.

It is worthy to highlight that since the crystalline structures of the TiC_x ancillary phase formed during the SPS synthesis and the Ti–C layer in the Ti_3AlC_2 are nearly identical; as such the differences in their chemical properties are negligible. Thus, TiC_x impurities are not expected to have an influence on the electrochemical corrosion properties of Ti_3AlC_2 [28].

3.3.1. Top-surface morphology and chemistry

Scanning electron micrograph of the top-surface is shown in Fig. 3. As shown, the top surface appears to be very rough with corrosion products deposited on the surface. Also, grain delamination and some micro pits are clearly evident at the surface post corrosion. Semi-quantitative elemental composition after EDS map analysis of the top-surface is presented in Table 1. The fraction of Al at the top-surface is very low, indicating a significant loss from the surface of the Ti_3AlC_2 MAX phase material. The oxygen fraction is somewhat high; it is suspected that this might be due to absorbed water in the remaining salt which is still present at the surface. The presence of chloride further supports that the salt at the surface would absorb moisture from the atmosphere - leading to high oxygen content. The significant Fe content is most likely due to material from the vessel lid spalling and subsequently falling into the crucible during the experiment.

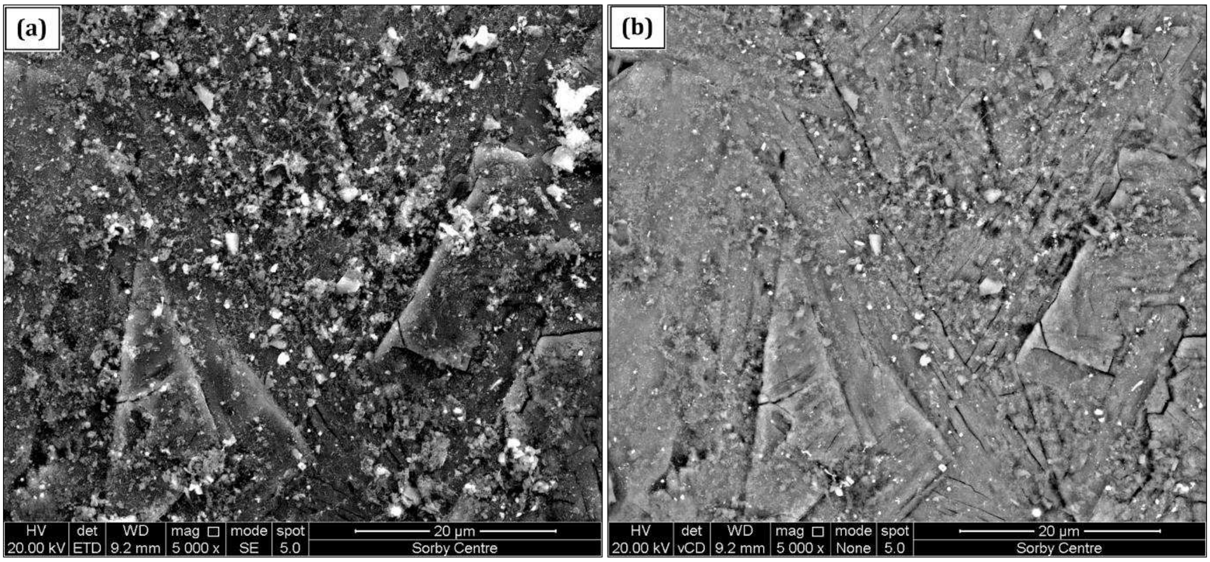

Fig. 3. (a) Secondary electron (SE), and (b) corresponding backscattered electron (BSE) micrographs taken from the top-surface after high-temperature corrosion in molten salt.

Glancing angle X-Ray diffraction (GAXRD) patterns normalized relative to the TiC(200) peak are shown in Fig. 4. TiC was the most intense phase at all glancing angles. The Ti_3AlC_2 phase peaks are relatively weak and the majority of these peaks vanished as the glancing angle was decreased to < 5° ω. The additional unknown peaks observed at glancing angle < 10° ω appear to correspond to $Ti_3C_2Cl_2$ phase, and is in agreement with observations reported elsewhere [37]. This is further supported by the fact that the [002] peaks of $Ti_3C_2[T_x]$ are inclined to shift towards smaller angles and broadens in contrast to that from Ti_3AlC_2 [38].

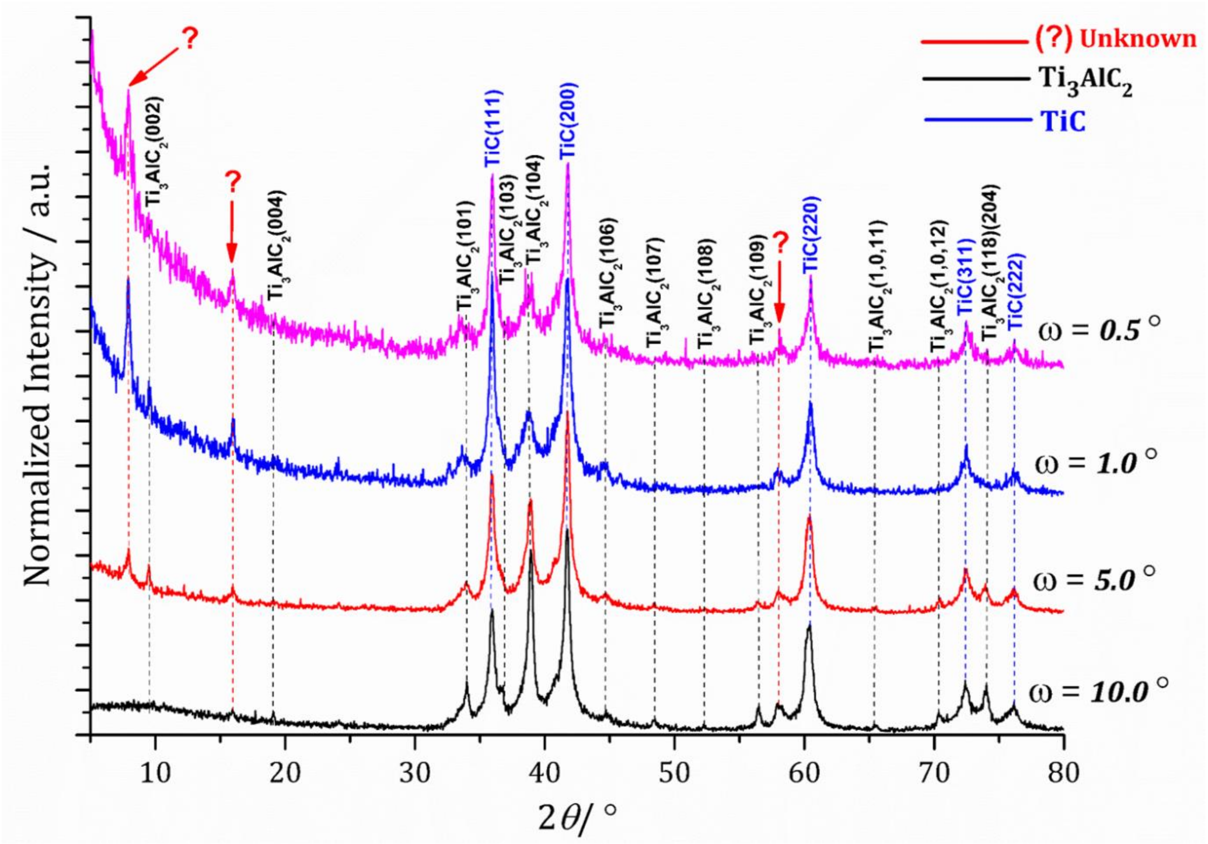

Fig. 4. GAXRD patterns after exposure to eutectic LiCl-KCl molten salt at 600 °C for 125 hours. Note the evolution of the $Ti_3C_2Cl_2$ phase at glancing angle < 10° ω. The unknown peaks are speculated to be that of $Ti_3C_2Cl_2$.

3.3.2. Cross-sectional morphology and chemistry

Cross-sectional morphologies from the surface exposed to the molten salt at 600 °C for 125 h is presented in Fig. 5. The reaction layer as measured from the SEM image was ~ 80 – 120 µm thick. Fig. 5(a and b) are comparative secondary electron (SE) and backscattered electron (BSE) SEM micrographs showing the extent of the reaction layer as well as evidence of grain exfoliation and delamination. Fig. 5(c) is a higher magnification BSE image of a Ti_3AlC_2 grain where extensive exfoliation of individual layers is evident. Fig. 5(d) is a BSE image that further reveals the exfoliated layer speculated to be $Ti_3C_2Cl_2$ (white arrow) alongside with non-stoichiometric TiC_x (red arrow) in agreement with the glancing angle XRD in Fig. 4.

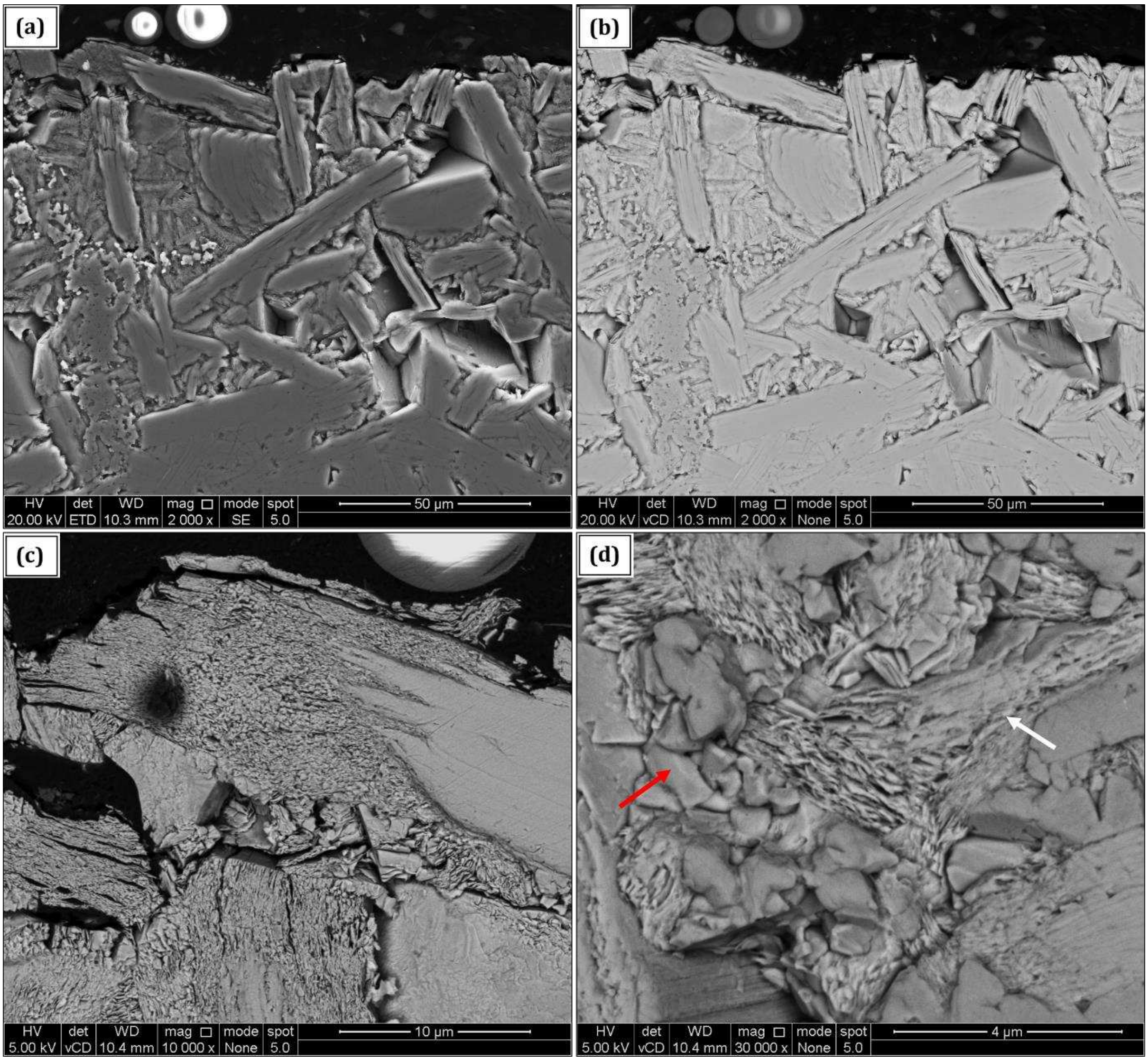

Fig. 5. SEM cross-section morphologies of corroded Ti_3AlC_2 showing: (a–b) secondary electron and corresponding backscattered electron images of the reaction layer, (c) backscattered image showing exfoliated Ti_3AlC_2 grain and (d) backscattered image showing the corrosion product ($TiC_{0.67}$) in red arrow and exfoliated layer $Ti_3C_2Cl_2$ in white arrow.

EDS elemental maps obtained from Fig. 5(b) is shown in Fig. 6. The annotations mark the location of point analyses, the compositions of which are presented in Table 1. According to the elemental map, three distinct phases were present. The first is that of the underlying substrate Ti_3AlC_2, which is clearly visible from the Al map. The second is TiC_x, which is distinguishable from a lack of lack of O, Al and Cl. The third is the Ti-C-Cl phase, which is most easily distinguished by the presence of Cl. However, it is worth mentioning that an additional phase possibly Ti-C-O-Cl already reported elsewhere [38, 39] may also coexist due to the presence of O in the Ti-C-Cl phase region as seen in the overlayed EDS map even though the EDS point spectrum (not shown) did not detect oxygen peak. EDS point analyses from the point (3) spectrum suggest that the approximate stoichiometry of this phase is Ti_2C_3Cl. This is contrary to the $Ti_3C_2Cl_2$ has speculated following the glancing angle XRD analyses. The reason for this is not fully understood at this time but it is conceivable that both phases do coexist. This is because following aluminium extraction, chlorine may have reacted with the exposed titanium which then subsequently dissolves in the melt to leave behind a carbide-derived carbon as observed elsewhere [40, 41]. It is therefore plausible that this carbide-derived carbon layer is responsible for the greater fraction of carbon than titanium in the exfoliated layer.

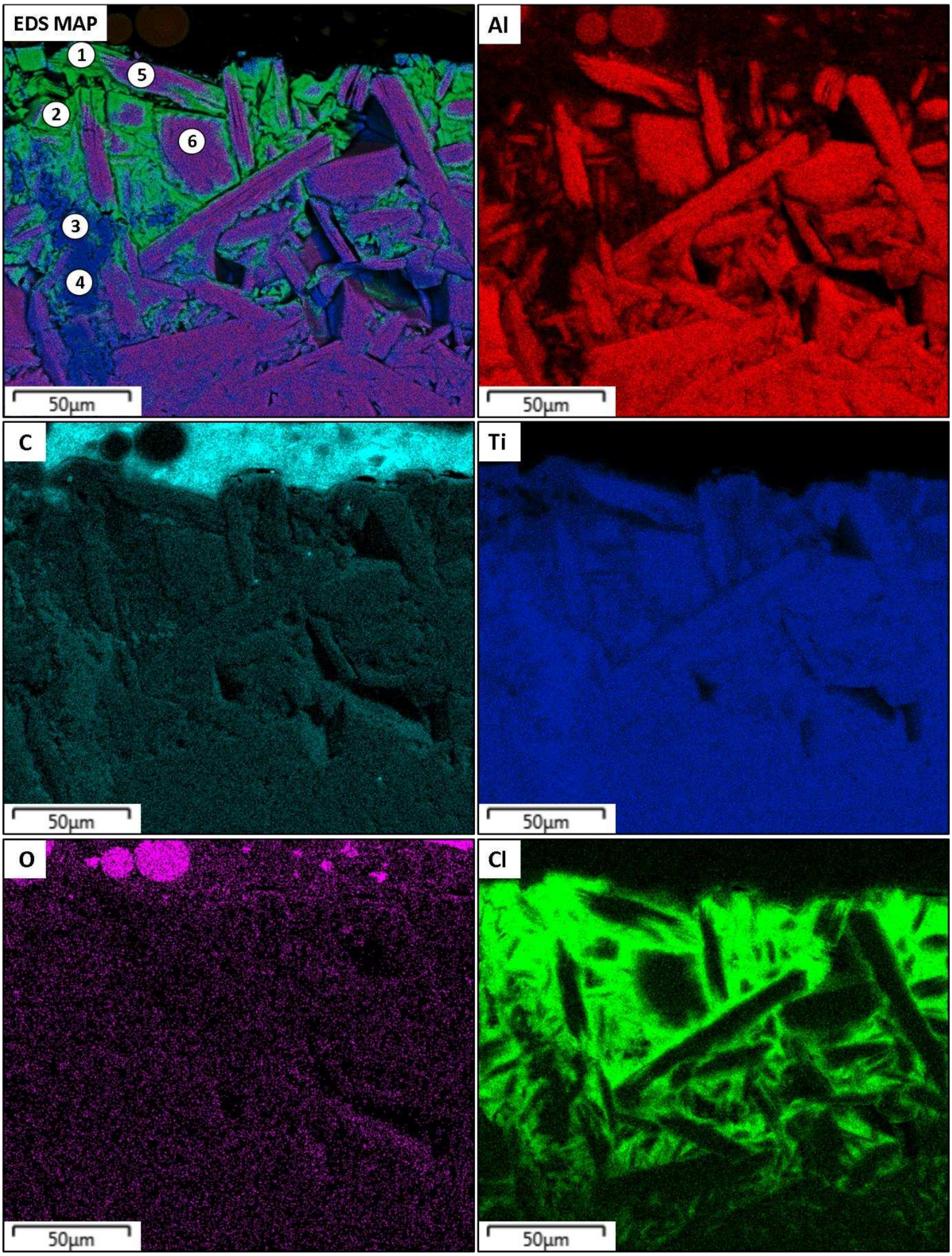

Fig. 6. EDS elemental maps from the cross-section. The top of the image is the sample surface. The layered map shows three distinct morphologies: Ti_3AlC_2, TiC_x and Ti-C-Cl phase. The annotations mark the locations of elemental point analyses shown in Table 1. Note some traces of Fe was also seen in the map spectrum although not shown here.

Table 1. Top-surface and cross-sectional elemental composition (at.%) of Ti_3AlC_2 after corrosion in LiCl-KCl molten salt at 600 °C for 125 hours

TOP SURFACE							
O	**Ti**	**C**	**Fe**	**Cl**	**Al**	**Others**	**Elements**
37.7	33.4	18.3	4.5	4.2	0.9	0.8	S,Si,K,P,Cu

CROSS SECTION						
SPECTRUM	**Ti**	**Al**	**C**	**Cl**	**Others**	**Elements**
Point 1	32.4	0.2	48.0	18.8	0.6	Fe,Ca,K,Si
Point 2	34.5	0.7	47.4	16.7	0.7	Fe,K,Si
Point 3	54.4	0.1	45.2	0.2	0.1	Si
Point 4	55.6	0.2	43.8	0.1	0.3	Ni,W
Point 5	48.2	14.6	36.3	0.2	0.7	Fe,Cu,Ca
Point 6	49.2	14.8	35.7	0.1	0.1	Fe

3.4. Ti_3AlC_2 response to high temperature molten salt

The Ti_3AlC_2 structure is composed of individual Ti_3C_2 layers separated by Al atoms. Following the exposure to LiCl-KCl molten salt, the generation of Cl_2 provides the driving force for selective out-diffusion of Al atoms from between the layers; as a result, this brings about the exfoliation of individual Ti_3C_2 layers from each other owing to the loss of metallic bonding holding them together. The loss of aluminium from the A–atom plane leaves behind $M_{n+1}X_n$ sheets separated from each other and their surfaces [42] which are then immediately functionalized by surface terminating species, T_x, emanating from the molten salt to form $M_{n+1}X_nT_x$ [43, 44]. As such the inward-diffusing Cl^- anions will spontaneously intercalate into the A–site plane vacated by the Al atoms and bond between Ti_3C_2 sublayers to form a more stable phase $Ti_3C_2Cl_2$ [37]. Thus the corrosion products are $TiC_{0.67}$ rock salt structure [45, 46] and the exfoliated layer $Ti_3C_2Cl_2$ [37, 47]. Exfoliation is particularly evident judging from the diffraction patterns (Fig. 4) that reveals a weakening diffraction signal of the non-basal plane peaks of Ti_3AlC_2, most notably the most intense peak at ≈ 39° 2θ.

The M–A bonding energy in the MAX crystal structure plays a vital role in relation to the ease of removal of the A–element. Some MAX phases, such as V_2AlC and Nb_2AlC have been reported to possess higher bonding energy; as a result, longer time is required to remove the A-atoms [44]. As the M–A bond energies in MAX phases are different, it is conceivable that the weak M–Al bonding in Ti_3AlC_2 [48] favoured the ease of extraction of Al atoms from the two-dimensional A–site plane which was then subsequently dissolved in the molten salt. The formation of $AlCl_3$ vapour is also probable as its boiling point is 180 °C. However it is more likely that it would interact with LiCl and KCl and stay in the melt as $AlCl_4$.

The A–layer has been established to play a dominant role in the corrosion behaviour of MAX phases; and certain grain orientations which expose the A–layer are more likely to corrode due to ease of Al de-intercalation [49]. When the basal planes are perpendicular to the surface the A–layers are exposed. On the other hand, when the basal planes are parallel to the surface (i.e. basal textured sample) the A–layers are shielded [49]. Irrespective of the M–A bonding energy and grain orientation, the main reason behind the poor corrosion resistance of Ti_3AlC_2 in this study was the lack of formation of an Al_2O_3 scale layer at the surface. The excellent high-temperature oxidation resistance of Ti_3AlC_2 can be partly blamed for this [50]. The formation temperature of α–Al_2O_3 is reported to be above 900 °C [51]; and as Al is continuously extracted from Ti_3AlC_2 following exposure to the molten salt below this temperature, it is clear that all the Al would have been extracted before the Al_2O_3 formation temperature is attained. Protective alumina scales have been reported to be an effective barrier to the inward penetration of chloride and chloride molten salts [52]. Thus pre-oxidation is needed prior to exposure to molten salt to aid the formation of an Al_2O_3 scale. Previous work by Lin et al. [51] showed that pre-oxidation in air at 1000 °C inhibited the infiltration of molten salt into a Ti_2AlC substrate due to the formation of a continuous Al_2O_3 scale.

It is also worth mentioning that a possible galvanic cell that might have developed owing to contact between the MAX phase material and the materials used in the experimental set-up, that is, steel bar and nickel wire cannot be ruled out despite attempts to mitigate this using mica to insulate the sample. This might have exacerbate the extent of corrosion especially via the oxidation of chloride ion to chlorine gas. Whilst this does not alter the underlying corrosion mechanism, it does highlight a technological challenge in employing MAX phases in a molten salt reactor that often incorporates a range of dissimilar materials in its architecture.

3.4.1 Ti_3AlC_2/LiCl-KCl corrosion mechanism

When in contact with the molten salt it appears that a chemical driving force induces the extraction and migration of Al from the A-atom site plane in Ti_3AlC_2. Although the mechanism behind the chemical driving force is not fully understood, however, according to Barsoum et al. [45] it is plausible that the reaction of Al with dissolved oxygen in the molten bath plays a role in this mechanism. The continuous extraction of Al from the A-atom site leave behind a twinned and relaxed Ti_3C_2 layers that is spontaneously terminated by Cl^- ions to form a stable $Ti_3C_2Cl_2$ [37]. However, some of the Ti_3C_2 layers are not transformed into $Ti_3C_2Cl_2$ as it would be expected but instead into non-stoichiometric TiC_x. A major reason for this deviation is the possible de-twinning of the as relaxed Ti_3C_2 layers due to oxygen incorporation [39, 46]. According to Barsoum et al. [45] and Emmerlich et al. [46] not all Ti_3C_2 layers are terminated by the Cl^- ions as an inward diffusing O (evident from the EDX map) may occupy the empty A-site vacated by the Al atoms to bring about detwinning of the as relaxed Ti_3C_2 layers into non-stoichiometric $TiC_{0.67}$. The formation of non-stoichiometric $TiC_{0.67}$ is further supported by the increase in the intensity of the TiC peaks as observed from the glancing angle XRD patterns obtained from the cross-section of the sample post corrosion in Fig. 4. According to Lu et al. [53] and Urbankowski et al. [43], whilst Cl termination bonds well with the Ti_3C_2 surface, they are not as competitive as O-containing terminals. Thus a small part of the Cl terminations can be easily substituted by O-containing terminals during sample preparation processes such as water washing.

4. Conclusions

The following salient conclusions are reached upon spark plasma sintering of Ti_3AlC_2 MAX phase material and subsequent exposure to eutectic LiCl-KCl molten salt at 600 °C:

- Nearly single phase Ti_3AlC_2 MAX phase was synthesized by spark plasma sintering (SPS) under vacuum condition.
- Ancillary phase TiC_x coexisted in the final sintered product due to de-intercalation of aluminium to bring about a phase transformation from hexagonal phase Ti_3AlC_2 to cubic phase $TiC_{0.67}$.
- Ti_3AlC_2 is susceptible to chloride attack from the molten salt due to the selective extraction of Al from the basal plane leaving behind a relaxed Ti_3C_2 and its subsequent chlorination to $Ti_3C_2Cl_2$.
- De-twinning of the as relaxed Ti_3C_2 layers due to O incorporation led to non-stoichiometric $TiC_{0.67}$ formation.
- It is possible to mitigate Al extraction by synthesizing textured Ti_3AlC_2 with basal plane parallel to the surface, thus shielding the Al–layer and/or appropriate pre-oxidation to form alumina scale that is impregnable to chloride attack.

Acknowledgements

We wish to acknowledge the Henry Royce Institute for Advanced Materials, funded through EPSRC grants EP/R00661X/1, EP/S019367/1, EP/P02470X/1 and EP/P025285/1. Authors are grateful to EPSRC for funding through the Nuclear First DTC programme. Authors wish to acknowledge the support of Seaborg. We further acknowledge University of Sheffield Knowledge Exchange Scholarship 19/20 funded by the EPSRC Impact Acceleration Account.

Data availability

The raw/processed data required to reproduce these findings are available to download from the white rose e-thesis from: http://etheses.whiterose.ac.uk/24202/

References

1. G.F. Flanagan, D.E.H., and S.M. Cetiner, Report No. ORNL/TM-2012/226. June 2012, Oak Ridge National Laboratory: Oak Ridge, TN,.
2. D.E. Holcomb, G.F.F., G.T. Mays, W.D. Pointer, K.R. Robb, and G.L. Yoder, Report No. ONRL/TM-2013/401. September 2013, Oak Ridge National Laboratory: Oak Ridge, TN.
3. Zheng, G. and K. Sridharan, Corrosion of Structural Alloys in High-Temperature Molten Fluoride Salts for Applications in Molten Salt Reactors. JOM, 2018. **70**(8): p. 1535-1541.
4. Delpech, S., C. Cabet, C. Slim, and G.S. Picard, Molten fluorides for nuclear applications. Materials Today, 2010. **13**(12): p. 34-41.
5. Olson, L.C., J.W. Ambrosek, K. Sridharan, M.H. Anderson, and T.R. Allen, Materials corrosion in molten LiF–NaF–KF salt. Journal of Fluorine Chemistry, 2009. **130**(1): p. 67-73.
6. Busby, J., L. Garrison, L. Lin, S. Raiman, S. Sham, C. Silva, H. Wang, and R.N. ORNL/SPR-2019/1089, Technical Gap Assessment for Materials and Component Integrity Issues for Molten Salt Reactors. 2019, Oak Ridge National Laboratory Materials Science and Technology Division: Oak Ridge TN. p. 156.
7. Ye, X.X., H. Ai, Z. Guo, H. Huang, L. Jiang, J. Wang, Z. Li, and X. Zhou, The high-temperature corrosion of Hastelloy N alloy (UNS N10003) in molten fluoride salts analysed by STXM, XAS, XRD, SEM, EPMA, TEM/EDS. Corrosion Science, 2016. **106**: p. 249-259.
8. Ren, W., G. Muralidharan, D. Wilson, and D. Holcomb, Considerations of Alloy N for Fluoride Salt-Cooled High-Temperature Reactor Applications. 2011.
9. Koger, J.W., Evaluation of Hastelloy N alloys after nine years exposure to both a molten fluoridesalt and air at temperatures from 700 to 560°C, ORNL-TM-4189, 1972. Oak Ridge National Laboratory.
10. Fukumoto, K.I., R. Fujimura, M. Yamawaki, and Y. Arita, Corrosion behavior of Hastelloy-N alloys in molten salt fluoride in Ar gas or in air. Journal of Nuclear Science and Technology, 2015. **52**(10): p. 1323-1327.
11. R. N. Wright, T.L.S., Report No. INL/EXT-18-45171, Status of Metallic Structural Materials for Molten Salt Reactors. May 2018: Idaho National Laboratory, Idaho Falls, Idaho.
12. Hoffman, E.N., D.W. Vinson, R.L. Sindelar, D.J. Tallman, G. Kohse, and M.W. Barsoum, MAX phase carbides and nitrides: Properties for future nuclear power plant in-core applications and neutron transmutation analysis. Nuclear Engineering and Design, 2012. **244**: p. 17-24.
13. Xiao, J., T. Yang, C. Wang, J. Xue, and Y. Wang, Investigations on Radiation Tolerance of $M_{n+1}AX_n$ Phases: Study of Ti_3SiC_2, Ti_3AlC_2, Cr_2AlC, Cr_2GeC, Ti_2AlC, and Ti_2AlN. Journal of the American Ceramic Society, 2015. **98**(4): p. 1323-1331.

14. Huang, Q., R. Liu, G. Lei, H. Huang, J. Li, S. He, D. Li, L. Yan, J. Zhou, and Q. Huang, Irradiation resistance of MAX phases Ti_3SiC_2 and Ti_3AlC_2: Characterization and comparison. Journal of Nuclear Materials, 2015. **465**: p. 640-647.
15. Barsoum, M.W., MAX phases : properties of machinable ternary carbides and nitrides. 2013: Weinheim, Germany : Wiley-VCH Verlag GmbH & Co. KGaA, 2013.
16. Sun, Z.M., Progress in research and development on MAX phases: a family of layered ternary compounds. International Materials Reviews, 2011. **56**(3): p. 143-166.
17. Barsoum, M. and M. Radovic, Mechanical Properties of the MAX Phases. Vol. 41. 2011. 195-227.
18. Barsoum, M.W. and T. El-Raghy, The MAX Phases: Unique New Carbide and Nitride Materials: Ternary ceramics turn out to be surprisingly soft and machinable, yet also heat-tolerant, strong and lightweight. American Scientist, 2001. **89**(4): p. 334-343.
19. Bowden, D., J. Ward, S. Middleburgh, S. de Moraes Shubeita, E. Zapata-Solvas, T. Lapauw, J. Vleugels, K. Lambrinou, W.E. Lee, M. Preuss, and P. Frankel, The stability of irradiation-induced defects in Zr_3AlC_2, Nb_4AlC_3 and $(Zr_{0.5},Ti_{0.5})_3AlC_2$ MAX phase-based ceramics. Acta Materialia, 2020. **183**: p. 24-35.
20. Tallman, D.J., E.N. Hoffman, E.a.N. Caspi, B.L. Garcia-Diaz, G. Kohse, R.L. Sindelar, and M.W. Barsoum, Effect of neutron irradiation on select MAX phases. Acta Materialia, 2015. **85**: p. 132-143.
21. Tallman, D.J., On the Potential of MAX phases for Nuclear Applications in Department of Materials Science and Engineering. June 2015, Drexel University p. 237.
22. Córdoba, J.M., M.J. Sayagués, M.D. Alcalá, and F.J. Gotor, Synthesis of Ti_3SiC_2 Powders: Reaction Mechanism. Journal of the American Ceramic Society, 2007. **90**(3): p. 825-830.
23. Magnuson, M. and M. Mattesini, Chemical bonding and electronic-structure in MAX phases as viewed by X-ray spectroscopy and density functional theory. Thin Solid Films, 2017. **621**: p. 108-130.
24. Wang, X.H. and Y.C. Zhou, High-Temperature Oxidation Behavior of Ti_2AlC in Air. Oxidation of Metals, 2003. **59**(3): p. 303-320.
25. Gupta, S., D. Filimonov, T. Palanisamy, and M.W. Barsoum, Tribological behavior of select MAX phases against Al_2O_3 at elevated temperatures. Wear, 2008. **265**(3): p. 560-565.
26. Sun, D., A. Zhou, Z. Li, and L. Wang, Corrosion behavior of Ti_3AlC_2 in molten KOH at 700 °C. Journal of Advanced Ceramics, 2013. **2**(4): p. 313-317.
27. Li, D., Y. Liang, X. Liu, and Y. Zhou, Corrosion behavior of Ti_3AlC_2 in NaOH and H_2SO_4. Journal of the European Ceramic Society, 2010. **30**(15): p. 3227-3234.
28. Zhu, M., R. Wang, C. Chen, H.B. Zhang, and G.J. Zhang, Comparison of corrosion behavior of Ti_3SiC_2 and Ti_3AlC_2 in NaCl solutions with Ti. Ceramics International, 2017. **43**(7): p. 5708-5714.
29. LI Ling, Y.G., Zhou Xingtai, Corrosion behaviour of Ti_3SiC_2 and Ti_3AlC_2 with LiF-NaF-KF molten salt. Nuclear Techniques, 2014. **37**(06): p. 60602-060602.
30. Naguib, M., V. Presser, D. Tallman, J. Lu, L. Hultman, Y. Gogotsi, and M.W. Barsoum, On the Topotactic Transformation of Ti_2AlC into a Ti–C–O–F Cubic Phase by Heating in Molten Lithium Fluoride in Air. Journal of the American Ceramic Society, 2011. **94**(12): p. 4556-4561.
31. Cooper, D., Feasibility of using MAX phase materials in molten salt reactors, in Department of Materials Science and Engineering. 2019, University of Sheffield: Sheffield, UK. p. 338.
32. Jantzen, C., An Investigation of Primary Circuit Materials in Molten Chloride Salts with the Design of High Temperature Corrosion Vessels, in School of Mechanical, Aerospace and Civil Engineering, The University of Manchester. 2019. p. 2553.
33. Zhou, Y. and Z. Sun, Crystallographic relations between Ti_3SiC_2 and TiC. Material Research Innovations, 2000. **3**(5): p. 286-291.
34. Ma , X.L., Y.L. Zhu, X.H. Wang, and Y.C. Zhou, Microstructural characterization of bulk Ti_3AlC_2 ceramics. Philosophical Magazine, 2004. **84**(28): p. 2969-2977.
35. Magnus, C. and W.M. Rainforth, Influence of sintering environment on the spark plasma sintering of Maxthal 312 (nominally-Ti_3SiC_2) and the role of powder particle size on densification. Journal of Alloys and Compounds, 2019. **801**: p. 208-219.

36. Magnus, C., J. Sharp, and W.M. Rainforth, The Lubricating Properties of Spark Plasma Sintered (SPS) Ti_3SiC_2 MAX Phase Compound and Composite. Tribology Transactions, 2019: p. 1-14.
37. Li, M., J. Lu, K. Luo, Y. Li, K. Chang, K. Chen, J. Zhou, J. Rosen, L. Hultman, P. Eklund, P.O.Å. Persson, S. Du, Z. Chai, Z. Huang, and Q. Huang, Element Replacement Approach by Reaction with Lewis Acidic Molten Salts to Synthesize Nanolaminated MAX Phases and MXenes. Journal of the American Chemical Society, 2019. **141**(11): p. 4730-4737.
38. Feng, W., H. Luo, Y. Wang, S. Zeng, L. Deng, X. Zhou, H. Zhang, and S. Peng, Ti_3C_2 MXene: a promising microwave absorbing material. RSC advances, 2018. **8**(5): p. 2398-243.
39. Naguib, M., V. Presser, D. Tallman, J. Lu, L. Hultman, Y. Gogotsi, and M.W. Barsoum, On the Topotactic Transformation of Ti_2AlC into a Ti-C-O-F Cubic Phase by Heating in Molten Lithium Fluoride in Air. Journal of the American Ceramic Society, 2011. **94**(12): p. 4556-4561.
40. Hoffman, E.N., G. Yushin, M.W. Barsoum, and Y. Gogotsi, Synthesis of Carbide-Derived Carbon by Chlorination of Ti_2AlC. Chem. Mater, 2005. **17**(9): p. 2317-2322.
41. Hoffman, E.N., G. Yushin, T. El-Raghy, Y. Gogotsi, and M.W. Barsoum, Micro and mesoporosity of carbon derived from ternary and binary metal carbides. Microporous and Mesoporous Materials, 2008. **112**(1): p. 526-532.
42. Naguib, M., M. Kurtoglu, V. Presser, J. Lu, J. Niu, M. Heon, L. Hultman, Y. Gogotsi, and M.W. Barsoum, Two-Dimensional Nanocrystals Produced by Exfoliation of Ti_3AlC_2. Advanced Materials, 2011. **23**(37): p. 4248-4253.
43. Urbankowski, P., B. Anasori, T. Makaryan, D. Er, S. Kota, P.L. Walsh, M. Zhao, V.B. Shenoy, M.W. Barsoum, and Y. Gogotsi, Synthesis of two-dimensional titanium nitride Ti_4N_3 (MXene). Nanoscale, 2016. **8**(22): p. 11385-11391.
44. Naguib, M., V.N. Mochalin, M.W. Barsoum, and Y. Gogotsi, 25th Anniversary Article: MXenes: A New Family of Two-Dimensional Materials. Advanced Materials, 2014. **26**(7): p. 992-1005.
45. Barsoum, M.W., T. El-Raghy, L. Farber, M. Amer, R. Christini, and A. Adams, The Topotactic Transformation of Ti_3SiC_2 into a Partially Ordered Cubic $Ti(C_{0.67}Si_{0.06})$ Phase by the Diffusion of Si into Molten Cryolite. Journal of The Electrochemical Society, 1999. **146**(10): p. 3919-3923.
46. Emmerlich, J., D. Music, P. Eklund, O. Wilhelmsson, U. Jansson, J.M. Schneider, H. Högberg, and L. Hultman, Thermal stability of Ti_3SiC_2 thin films. Acta Materialia, 2007. **55**(4): p. 1479-1488.
47. Li, Y., H. Shao, Z. Lin, J. Lu, L. Liu, B. Duployer, P.O.Å. Persson, P. Eklund, L. Hultman, M. Li, K. Chen, X.-H. Zha, S. Du, P. Rozier, Z. Chai, E. Raymundo-Piñero, P.L. Taberna, P. Simon, and Q. Huang, A general Lewis acidic etching route for preparing MXenes with enhanced electrochemical performance in non-aqueous electrolyte. Nature Materials, 2020. **19**(8): p. 894-899.
48. Chen, W., J. Tang, X. Shi, N. Ye, Z. Yue, and X. Lin, Synthesis and formation mechanism of high-purity Ti_3AlC_2 powders by microwave sintering. International Journal of Applied Ceramic Technology, 2020. **17**(2): p. 778-789.
49. Du, Y., J.X. Liu, Y. Gu, X.G. Wang, F. Xu, and G.J. Zhang, Anisotropic corrosion of Ti_2AlC and Ti_3AlC_2 in supercritical water at 500ºC. Ceramics International, 2017. **43**(9): p. 7166-7171.
50. Xu, X.W., Y.X. Li, J.Q. Zhu, and B.C. Mei, High-temperature oxidation behavior of Ti_3AlC_2 in air. Transactions of Nonferrous Metals Society of China, 2006. **16**: p. s869-s873.
51. Lin, Z., Y. Zhou, M. Li, and J. Wang, Hot corrosion and protection of Ti_2AlC against Na_2SO_4 salt in air. Journal of the European Ceramic Society, 2006. **26**(16): p. 3871-3879.
52. Li, Y.S. and M. Spiegel, Internal Oxidation of Fe–Al Alloys in a KCl-Air Atmosphere at 650°C. Oxidation of Metals, 2004. **61**(3): p. 303-322.
53. Lu, J., I. Persson, H. Lind, J. Palisaitis, M. Li, Y. Li, K. Chen, J. Zhou, S. Du, Z. Chai, Z. Huang, L. Hultman, P. Eklund, J. Rosen, Q. Huang, and P.O.Å. Persson, $Ti_{n+1}C_n$ MXenes with fully saturated and thermally stable Cl terminations. Nanoscale Advances, 2019. **1**(9): p. 3680-3685.